Journal of Alloys and Compounds 842 (2020) 155879

Contents lists available at ScienceDirect

Journal of Alloys and Compounds

journal homepage: http://www.elsevier.com/locate/jalcom

Controlled growth of single-crystalline $Bi_{.333}(Bi_6S_9)Br$ nanorods under hydrothermal conditions for enhanced photocatalytic reduction of Cr (VI)

Lili Ai , Dianzeng Jia **, Nannan Guo , Mengjiao Xu , Su Zhang , Luxiang Wang *, Lixia Jia

Key Laboratory of Energy Materials Chemistry, Ministry of Education Key Laboratory of Advanced Functional Materials, Autonomous Region Institute of Applied Chemistry, Xinjiang University, Urumqi, Xinjiang, 830046, China

ARTICLE INFO

Article history:
Received 13 February 2020
Received in revised form
23 May 2020
Accepted 31 May 2020
Available online 4 June 2020

Keywords:
$Bi_{.333}(Bi_6S_9)Br$
Nanorods
Photocatalysis
Cr (VI)

ABSTRACT

The rational design of composition and structure of the photocatalytic materials is especially critical for the practical application of photocatalytic technology. Herein, uniform single-crystal $Bi_{.333}(Bi_6S_9)Br$ nanorods were synthesized for the first time using a one-pot hydrothermal method. By prolonging the hydrothermal reaction time, the evolution process of $Bi_{.333}(Bi_6S_9)Br$ from nanoparticles to short nanorods, and finally to long nanorods was observed. $Bi_{.333}(Bi_6S_9)Br$ nanorods can effectively inhibit the recombination of photogenerated electron-hole pairs and effectively adsorb of Cr (VI) due to the presence of surface defects and unique structure, thereby promoting the photocatalytic activity. $Bi_{.333}(Bi_6S_9)Br$ nanorods exhibited excellent photocatalytic performance as well as promising recyclability in rapidly reducing aqueous Cr (VI) to Cr (III) under visible light. The degradation rate of Cr (VI) reached 90.96% within 60 min, and the structure of $Bi_{.333}(Bi_6S_9)Br$ did not change after six photocatalytic cycles. The photocatalytic reaction mechanism of nanorods was proposed based on the band structure of $Bi_{.333}(Bi_6S_9)Br$ and electron spin resonance radical scavenging assay.

© 2020 Elsevier B.V. All rights reserved.

1. Introduction

Photocatalysis using semiconductive oxides, sulfides *etc.* as active materials is one of the most promising approaches in tackling energy and environment problems [1,2]. While photocatalytic water splitting and CO_2 reduction remain highly challenging for practical applications, the degradation of harmful pollutants using photocatalysis has demonstrated high applicability for various organic compounds and inorganic cations [3–5]. For example, in wastewater treatment the abatement of heavy metal pollutants like hexavalent chromium Cr (VI) can be achieved by photocatalytic process [6–8]. It is noteworthy that Cr (VI) is extremely toxic to microorganisms as well as to human beings. Exposure to Cr (VI) may cause various health problems such as chromosome aberrations, digestive tract diseases, lung cancer, *etc* [9–11]. Up till now, titanium oxide- and zinc oxide-based semiconductor oxides are the most commonly used photocatalysts, which are typically effective under ultraviolet light due to their wide band gaps. Various doping and modifications have been performed to improve their quantum efficiency and spectral response range, which, however, remain as major challenges for their large scale applications [12,13]. Hence, more and more studies have been focusing on the exploration of alternative materials.

Recently, Bi-based semiconductors have received extensive attention due to their stable chemical structure and excellent photocatalytic performance [14,15]. Bismuth oxyhalides (BiOX, X = F, Cl, Br, I) as the most notable semiconductors among all bismuth compounds, consisting of $[Bi_2O_2]^{2+}$ layers sandwiched between two slabs of halogen ions [16–19]. As compared to oxide, bismuth oxyhalides exhibit a higher photocatalytic activity due to the presence of halogens. Another class of interesting Bi compounds in photocatalysis is bismuth chalcogenides, which have a good electrical conductivity, an outstanding thermoelectric performance and a narrow band gap [20–22]. For example, Luo and coworkers prepared hollow Bi_2S_3 nanospheres via Kirkendall effect, which was used for photocatalytic reduction of Cr (VI) in wastewater in electroplating industry and showed an outstanding performance [23]. Jin and coworkers reported Bi_2S_3 nanoribbons with

* Corresponding author.
** Corresponding author.
E-mail addresses: jdz0991@gmail.com (D. Jia), wangluxiangxju@163.com (L. Wang).

https://doi.org/10.1016/j.jallcom.2020.155879
0925-8388/© 2020 Elsevier B.V. All rights reserved.

different aspect ratios synthesized by solvothermal technique, and subsequent photocatalytic studies revealed that Bi_2S_3 nanocatalysts with the largest aspect ratio exhibited the highest activity in the reduction of CO_2 into methanol [24]. Wang et al. reported a general ionic-assisted microwave-ultrasonic combined synthetic strategy to fabricate Bi_2E_3 (E = S, Se, and Te) hierarchitectures, and the prepared hierarchical Bi_2S_3 nanospheres can be used in the actual Cr(VI)-containing wastewater treatment [25]. These promising results motivated us to work a step further in this direction, namely, to make use of the advantages of both oxyhalides and chalcogenides. It is believed that the halogens added to Bi chalcogenides will play an essential role in improving the photocatalytic activity of Bi chalcogenide like the BiOX system [26,27]. Nevertheless, bismuth sulfidehalides have been rarely reported in literatures so far.

In this work, the single-crystal $Bi_{.333}(Bi_6S_9)Br$ nanorods were synthesized by a one-pot hydrothermal method for the first time. The amount of raw materials used in this synthesis was calculated based on the stoichiometric ratio of Bi and S elements in $Bi_{.333}(Bi_6S_9)Br$. The effect of reaction time on the formation of nanorods was explored in detail, and the formation mechanism of nanorods was subsequently put forward. An outstanding photocatalytic performance was recorded in the reduction of Cr (VI) to Cr (III) under visible light irradiation. Moreover, the photocatalytic mechanism of the nanorods is proposed. The successful synthesis and application of the highly active single crystalline nanorods in this work may stimulate more studies on Bi-based photocatalysts.

2. Experimental

2.1. Synthesis of $Bi_{.333}(Bi_6S_9)Br$ nanorods

All chemicals are of analytical grade and used as received without further purification. $K_2Cr_2O_7$ (99.5%) was used to simulate wastewater in photocatalytic tests. The $Bi_{.333}(Bi_6S_9)Br$ nanorods were synthesized by a one-pot hydrothermal process. In a typical preparation process, 0.486 g of $Bi(NO_3)_3 \cdot 5H_2O$ (1 mmol) and 0.350 g of polyvinylpyrrolidone [$(C_6H_9NO)_n$, PVP] were dissolved into 25 mL of mannitol ($C_6H_{14}O_6$, 0.1 mol/L) solution under vigorous stirring. 5 mmol of NaBr was slowly added into the above mixture yielding a uniform reseda suspension. Afterwards, 1.4 mmol of thioacetamide (CH_3CSNH_2, TAA) was added to the above reseda suspension and vigorous stirring for 1 h for sulfuration. Subsequently, the mixture was sealed in a 50 mL Teflon-lined stainless-steel vessel and treated at 160 °C for 10 min, 1 h, 4 h and 8 h, respectively. The products were washed with distilled water, centrifuged and dried in a freeze drier. For comparison, pure oxyhalide (BiOBr) and pure chalcogenide (Bi_2S_3) were synthesized under the same hydrothermal conditions (160 °C for 4 h) except for the absence of TAA and NaBr, respectively.

2.2. Characterization

X-ray diffraction (XRD) was performed using a SmartLab-SE Diffractometer (Rigaku, Japan) with a Cu Kα radiation source (λ = 1.5406 Å). A field emission scanning electron microscopy (FESEM, Hitachi S-4800, Japan) was used to examine the morphology of the samples. The high resolution transmission electron microscopy (HRTEM) and corresponding Fast Fourier Transform (FFT), and high angle annular dark field-scanning transmission electron microscope (HAADF-STEM) were carried out with a JEM 2100F microscope equipped with an energy dispersive spectrometer (EDS). The solid-state diffuse reflectance spectra (DRS) and photoluminescence emission spectra (PL) were measured on a UV-vis spectrophotometer (Hitachi U-3010, Japan) and a fluorescence spectrophotometer (Hitachi F-4500, Japan), respectively. X-ray photoelectron spectroscopy (XPS, Thermo ESCALAB 250Xi, USA) was performed to investigate the surface chemical composition and binding state of the samples. The electron paramagnetic resonance (EPR) spectra were recorded on a Bruker EMX nano EPR spectrometer at 298 K, and electron spin resonance (ESR) spectra were obtained using an EPR spectrometer (JEOL JES-FA200, Japan) at the same temperature.

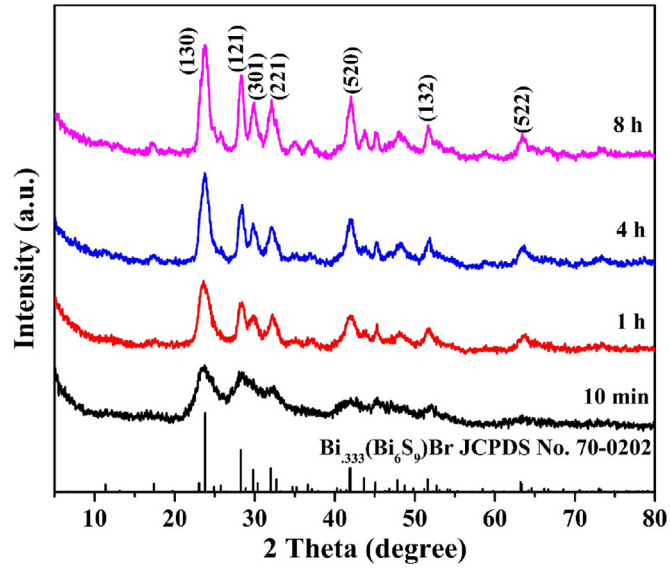

Fig. 1. XRD patterns of the as-prepared samples obtained by hydrothermal reaction for different reaction durations.

2.3. Photocatalytic activity evaluation

A photocatalytic reaction system (Xujiang Electromechanical Plant, Nanjing, China) was used to evaluate the photocatalytic reduction of Cr (VI) under visible light illumination from a 300 W Xenon lamp with a 420 nm cutoff filter (about 11 mW/cm^2). In a typical process, 10 mg of photocatalyst was added into a quartz tube reactor containing 50 mL of Cr (VI) solution (10 mg L^{-1} based on Cr in a dilute $K_2Cr_2O_7$ solution). In order to ensure the establishment of an adsorption-desorption equilibrium, the suspension was sonicated for 10 min and magnetically stirred in the dark for 30 min before irradiation. During the reaction process, 2 mL aliquot of the suspension was taken out at given time intervals. The supernatant liquid was obtained after centrifugation and used for further analysis. The concentration of Cr (VI) ions in the supernatant was determined by the diphenylcarbazide (DPC) method (see Supporting Information) and the corresponding UV-vis absorption spectra were recorded on a UV-vis spectrophotometer. After each reaction cycle, the photocatalyst was separated by centrifugation and employed for Cr abatement in a fresh Cr (VI) solution (10 mg L^{-1}). Parallel experiments were performed to obtain enough catalysts for the reuse.

3. Results and discussion

3.1. Characterization of $Bi_{.333}(Bi_6S_9)Br$ samples

The XRD patterns of the samples obtained by hydrothermal reaction at 160 °C for different reaction durations are shown in Fig. 1. All the reflections of the samples can be readily assigned to the hexagonal $Bi_{.333}(Bi_6S_9)Br$ (JCPDS card No. 70-0202, space group P63/(173), $a = b = 15.545$ Å, $c = 4.019$ Å, $\alpha = \beta = 90°$, $\gamma = 120°$). It

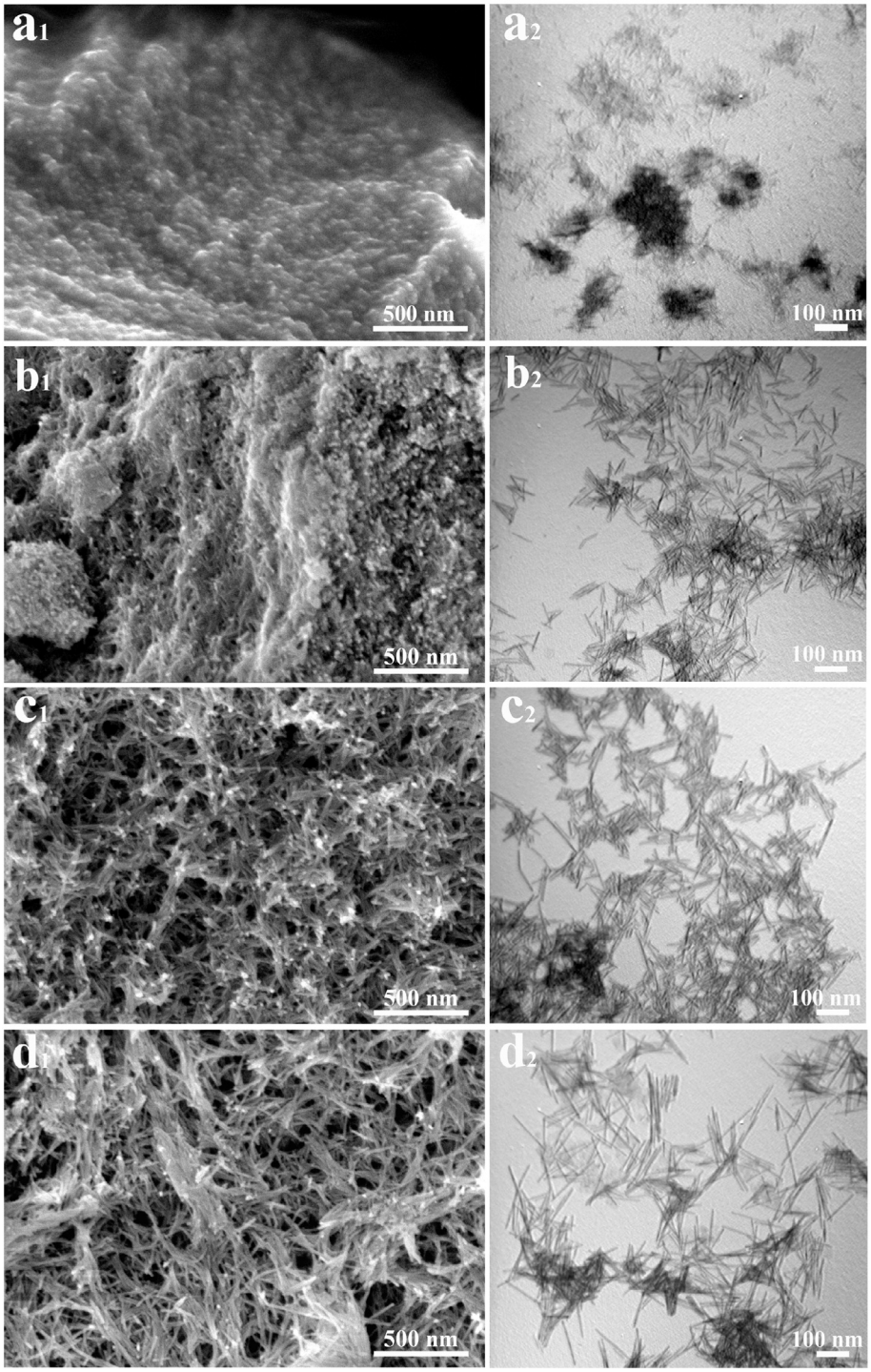

Fig. 2. FESEM images (a_1-d_1) and TEM images (a_2-d_2) of $Bi_{.333}(Bi_6S_9)Br$ nanorods synthesized by hydrothermal method for different reaction durations: (a) 10 min, (b) 1 h, (c) 4 h and (d) 8 h.

can be seen from the XRD patterns that with increasing reaction time the reflections became stronger, and the full width at half maxima (FWHM) of diffraction peak of (130) facet became narrower, indicating continuous growth of crystals and increasing crystallinity. The crystal structure of $Bi_{.333}(Bi_6S_9)Br$ is depicted in Fig. S1. It consists of BiS_8 and $Bi(S_5Br_2)$ polyhedra, as well as BiS_8 and $Bi(S_5Br_2)$ polyhedra connected consecutively by coedges. The XRD results demonstrated that highly crystalline $Bi_{.333}(Bi_6S_9)Br$ can be prepared by stoichiometrically applying Bi and S elements in the raw materials during hydrothermal synthesis.

The development of the nanorods was evidenced by FESEM and TEM studies as shown in Fig. 2. Nanoparticles of $Bi_{.333}(Bi_6S_9)Br$ were formed initially and the nanoparticles tend to form short nanorods (Figs. 2a and 10 min), which were grown up into one dimensional short nanorods as the reaction time was extended to 1 h (Fig. 2b). As the reaction time increased further to 4 h, the length of the nanorods increased significantly (Fig. 2c). Finally, well-defined nanorods with high aspect ratios were obtained after reaction for

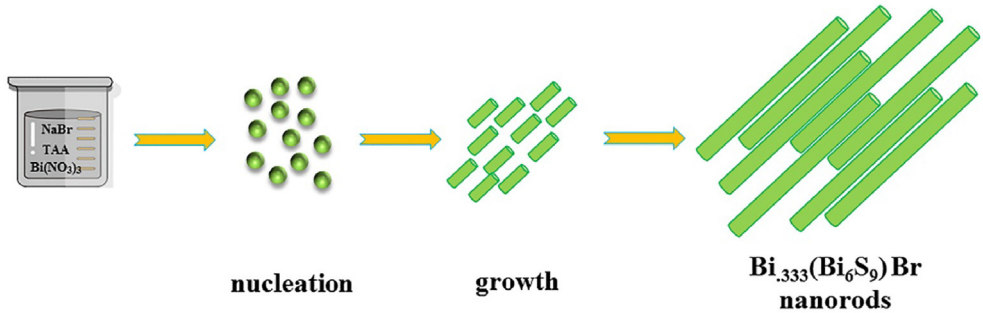

Fig. 3. Schematic illustration of the growth processes of the $Bi_{.333}(Bi_6S_9)Br$ nanorods.

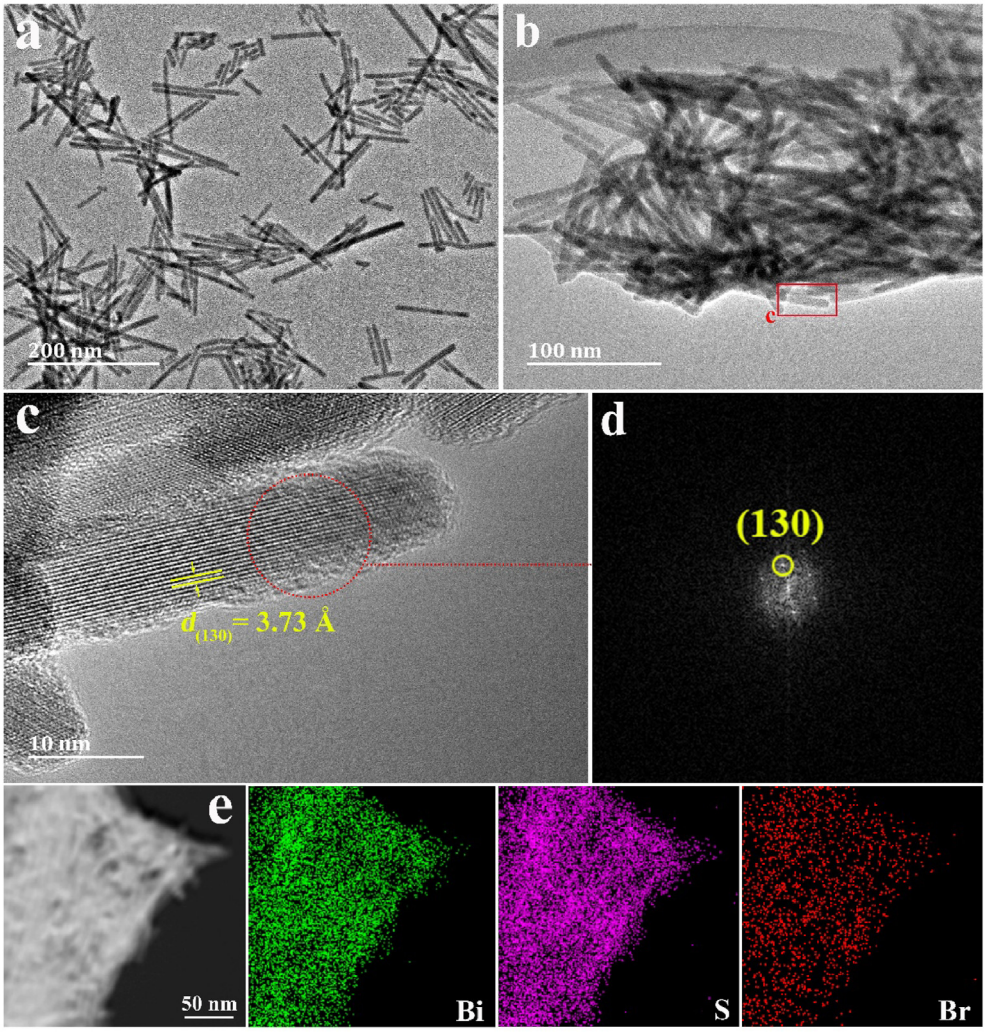

Fig. 4. Microscopic characterization of $Bi_{.333}(Bi_6S_9)Br$ nanorods: (a-b) TEM images, (c) HRTEM image, (d) FFT image, (e) HAADF-STEM image and EDS elemental mapping images.

8 h (Fig. 2d). Based on the above analysis, it can be concluded that the nanorods were formed through initial nucleation followed by anisotropic growth. The growth of the nanorods is schematically illustrated in Fig. 3. Firstly, the $Bi(NO_3)_3 \cdot 5H_2O$ was dissolved into mannitol solution and reacted with the large quantity of the Br^- and S^{2-} ion to form the $Bi_{.333}(Bi_6S_9)Br$ nucleates in the solution. Subsequently, the $Bi_{.333}(Bi_6S_9)Br$ nucleates could be further grown into nanoparticles under hydrothermal conditions, followed by the formation of short nanorods with increasing reaction time. The $Bi_{.333}(Bi_6S_9)Br$ nanorods with high aspect ratios and high crystallinity are finally formed after hydrothermal reaction for more than 4 h.

For photocatalysts, a larger particle size may increase the transport path and the recombination probability of photogenerated charge carriers, which are detrimental for photocatalytic reactions [28]. Thus, grain size is an important factor in photocatalysis. In this work, the microstructure of $Bi_{.333}(Bi_6S_9)Br$ obtained by hydrothermal reaction for 4 h was further analyzed in

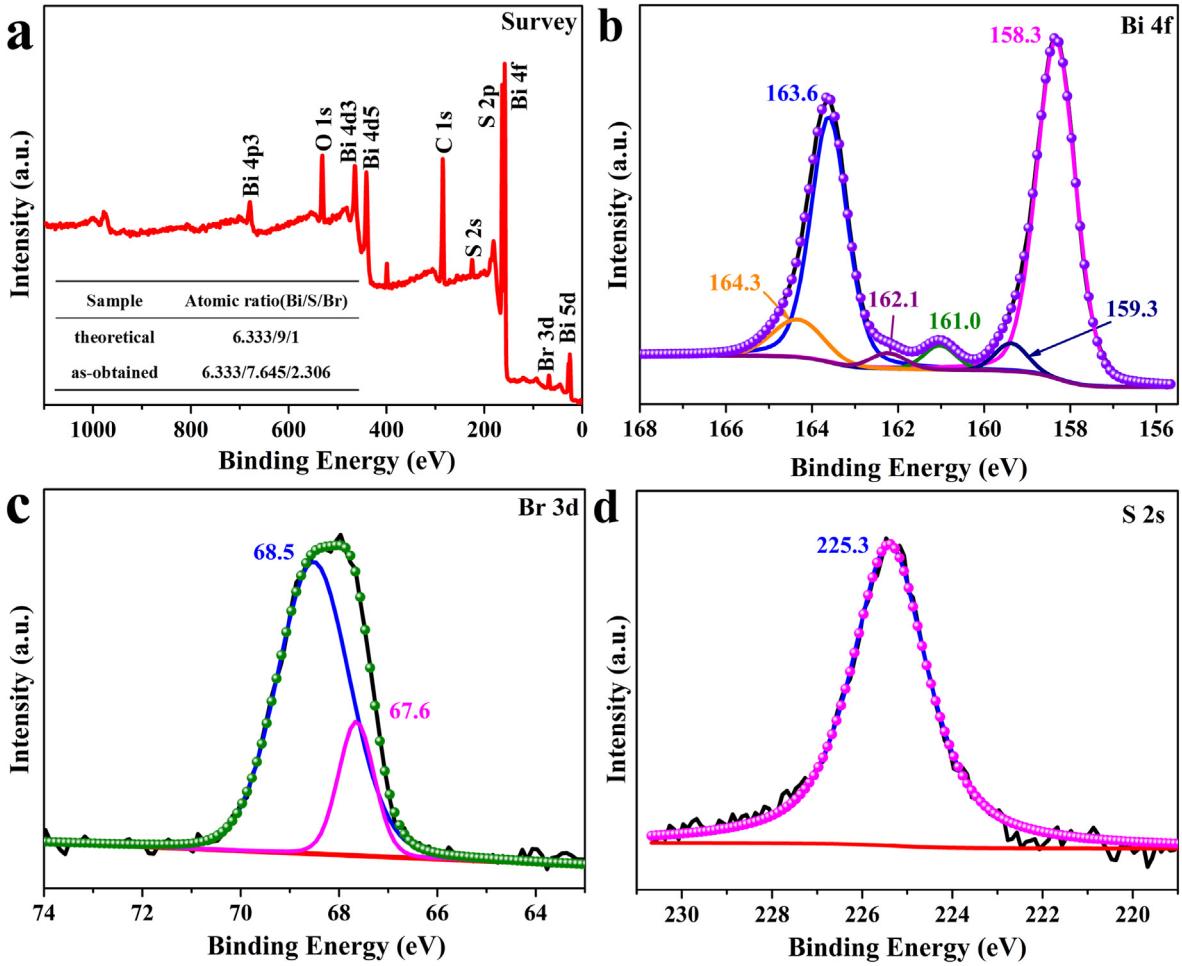

Fig. 5. XPS spectra of the as-prepared $Bi_{.333}(Bi_6S_9)Br$: (a) survey spectrum, (b) Bi 4f, (c) Br 3d, (d) S 2s.

detail. As shown in Fig. 4a and b, the TEM images demonstrate that the obtained $Bi_{.333}(Bi_6S_9)Br$ nanorods are homogeneous in shape and size with diameter of about 10 nm and a typical length of about 150 nm. The clear lattice fringes with a lattice spacing of 3.73 Å in HRTEM image corresponds to the (130) facet of $Bi_{.333}(Bi_6S_9)Br$ crystal (Fig. 4c), and the diffraction spot corresponding to the *d*-value of 3.73 Å can be observed in the FFT pattern (Fig. 4d). The corresponding EDS elemental mapping images reveal that the Bi, S and Br elements are evenly distributed throughout the whole nanorods (Fig. 4e).

The surface composition and chemical states of $Bi_{.333}(Bi_6S_9)Br$ were investigated by XPS. The survey XPS spectrum of the sample is shown in Fig. 5a, and there are no obvious impurities in the sample except for O and C, which are common for materials after exposure to ambient air. It was reported that surface defects could be evaluated by the Bi/S/Br ratio derived from XPS [29]. The Bi/S/Br atomic ratios of the as-obtained $Bi_{.333}(Bi_6S_9)Br$ differ greatly from the theoretical values as disclosed by XPS analysis (insert in Fig. 5a). The lower concentration of S element indicates the presence of sulfur vacancies in the surface region. Fig. 5b shows the high-resolution Bi 4f spectrum. The doublet at 158.3 and 163.6 eV of $Bi_{.333}(Bi_6S_9)Br$ can be assigned to Bi $4f_{7/2}$ and Bi $4f_{5/2}$, respectively [30–32]. The shoulder at higher binding energies may be tentatively assigned to Bi–S defect because the Bi–S defect is more electropositive than the lattice Bi and therefore appears at higher binding energies [33]. The binding energies located at 161.0 and 162.1 eV are well matching to the S $2p_{3/2}$ and S $2p_{1/2}$ peaks [33,34]. The Br 3d spectrum is deconvoluted into two peaks at 67.6 and 68.5 eV (Fig. 5c), which can be ascribed to Br $3d_{3/2}$ and Br $3d_{1/2}$, respectively [35,36]. The S 2s spectrum in Fig. 5d consists of a single peak at 225.3 eV, revealing the presence of the S^{2-} species [11,37].

The UV-vis DRS was used to investigate the optical properties of the $Bi_{.333}(Bi_6S_9)Br$ nanorods. As shown in Fig. S2a, the $Bi_{.333}(Bi_6S_9)Br$ shows strong photo absorption in both the ultraviolet and visible light regions. It is known that the band gap energy of the direct semiconductor is linearly proportional to the square of the absorption coefficient, and the indirect semiconductor band gap energy is linearly proportional to the square root of the absorption coefficient [2,38]. Analysis of the converted Kuberka-Munk function and light energy shows that the square of the absorption coefficient versus the energy function is more linear than the square root of the absorption coefficient versus the energy function (inset of Fig. S2a). We believe that the $Bi_{.333}(Bi_6S_9)Br$ catalyst is a direct band gap semiconductor. The band gap (E_g) of the as-prepared $Bi_{.333}(Bi_6S_9)Br$ nanorods is derived to be about 1.65 eV (inset of Fig. S2a). To further explore the band structure of $Bi_{.333}(Bi_6S_9)Br$, XPS valence band (VB) spectrum was collected and linearly extrapolated to determine the VB position (E_{VB}) of the sample. As displayed in Fig. S2b, the E_{VB} of $Bi_{.333}$ (Bi_6S_9) Br is about 0.91 eV vs. vacuum level. The E_{VB} vs. NHE could be calculated to be 0.86 eV according to the contact potential difference between the sample and the XPS analyzer. According to the equation $E_{CB} = E_{VB} - E_g$, the

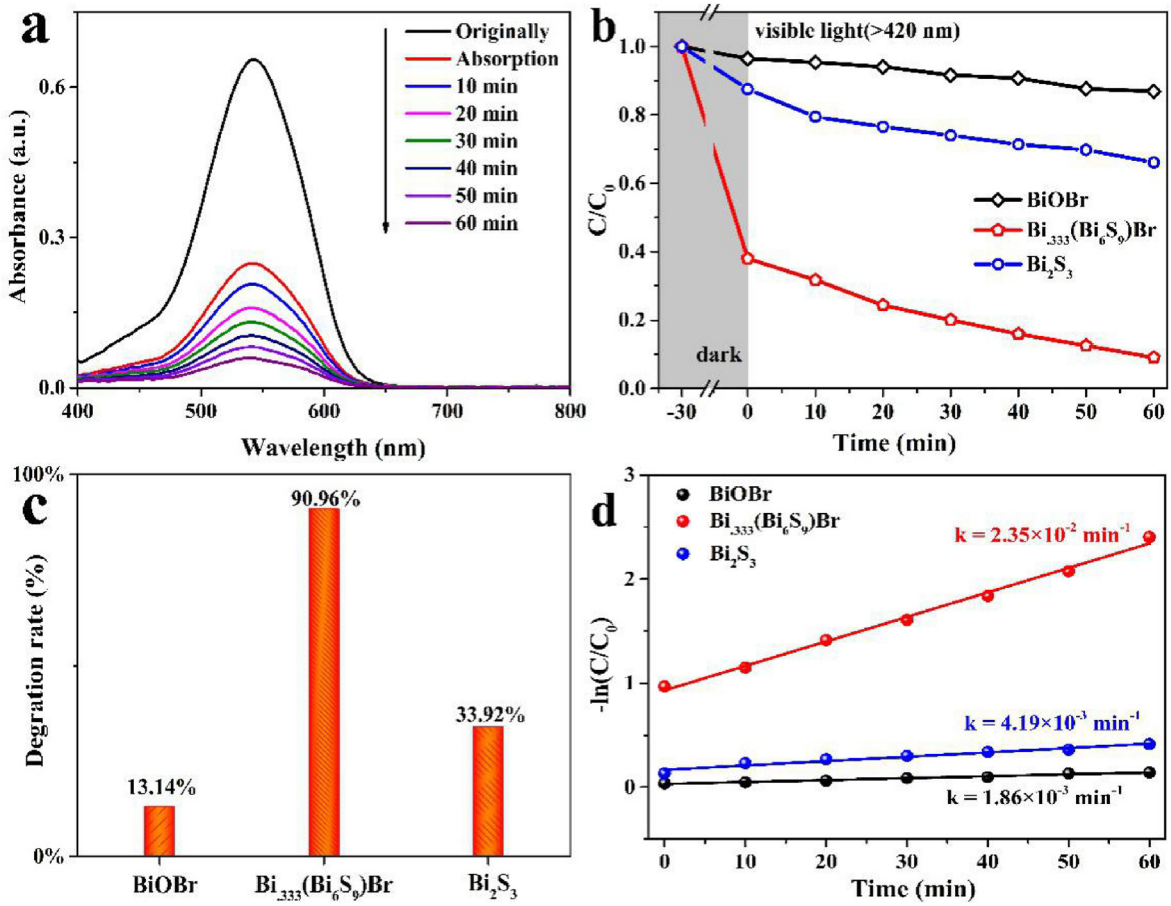

Fig. 6. (a) UV-vis absorption spectra of Cr (VI) solution as a function of reaction time using $Bi_{.333}(Bi_6S_9)Br$ (obtained at 160 °C for 4 h) as catalyst under visible light (>420 nm) irradiation; (b) Reduction curves of Cr (VI) derived from (a), BiOBr and Bi_2S_3 were also tested for comparison; (c) Degradation rate of Cr (VI) after reaction for 60 min, (d) Pseudo-first-order kinetics fitting curves.

corresponding conduction-band (CB) position (E_{CB}) of $Bi_{.333}(Bi_6S_9)Br$ is −0.79 eV.

3.2. Photocatalytic performance of $Bi_{.333}(Bi_6S_9)Br$ nanorods

To evaluate the photocatalytic performance of $Bi_{.333}(Bi_6S_9)Br$, the reduction of Cr (VI) was performed under visible light (>420 nm). Among all the samples, the one obtained by hydrothermal reaction at 160 °C for 4 h showed the highest conversion efficiency (Fig. S3). The sample obtained at 160 °C for 10 min is unstable under visible light irradiation because the crystal structure was destroyed after reaction (Fig. S4). It was demonstrated that different hydrothermal reaction time led to different grain size, and the effect of grain size on catalytic performance can be clearly seen from the catalytic tests. Obviously, the sample of 4 h outperformed other samples thanks to its grain size and unique structural and electronic properties related to its dimensions.

UV-vis absorption spectra of Cr (VI) solution were recorded at different time intervals during photocatalytic reduction using $Bi_{.333}(Bi_6S_9)Br$ (obtained at 160 °C for 4 h) as catalyst (Fig. 6a). For comparison, the photocatalytic performances of the BiOBr nanosheets and Bi_2S_3 nanorods (see XRD and FESEM results in Fig. S5) synthesized under the same conditions were also investigated. The concentration of Cr (VI) derived from the absorption spectra decreases with increasing reaction time (Fig. 6b). Moreover, adsorption of aqueous phase pollutants is also important for efficient photocatalytic process [39–43]. Compared to BiOBr and Bi_2S_3, $Bi_{.333}(Bi_6S_9)Br$ nanorods have the highest adsorption capacity in the dark, which may be due to the presence of surface defects on the $Bi_{.333}(Bi_6S_9)Br$ nanorods that enable to effectively adsorb and activate Cr (VI), thereby promoting the photocatalytic reaction. 90.96% of Cr (VI) was reduced to Cr (III) after 60 min using $Bi_{.333}(Bi_6S_9)Br$ as photocatalyst, while 13.14% and 33.92% were reduced at the same time using BiOBr and Bi_2S_3 as photocatalyst, respectively (Fig. 6c). In addition, the reduction curves of Cr (VI) catalyzed by $Bi_{.333}(Bi_6S_9)Br$, BiOBr and Bi_2S_3 after eliminating the adsorption are shown in Fig. S6. The $Bi_{.333}(Bi_6S_9)Br$ exhibits the best photocatalytic performance with 76.20% Cr (VI) reduction in 60 min after eliminating the adsorption. The plot of -ln (C/C_0) as a function of reaction time suggests that the Cr (VI) reduction reaction fits well with pseudo-first-order kinetics, i.e. $-\ln(C/C_0) = kt$, where C is the concentration of the Cr (VI) at time t, C_0 is the initial concentration of the Cr (VI) solution, and the slope k is the apparent reaction rate constant [11]. As shown in Fig. 6d, the k constant of $Bi_{.333}(Bi_6S_9)Br$ is determined to be 2.35×10^{-2} min^{-1}, which is 12.6 times that of BiOBr ($k = 1.86 \times 10^{-3}$ min^{-1}) and 5.6 times that of Bi_2S_3 ($k = 4.19 \times 10^{-3}$ min^{-1}), respectively. Compared with literature results (Table S1), the $Bi_{.333}(Bi_6S_9)Br$ sample shows great advantages in the photocatalytic reduction of Cr (VI).

The recyclability and stability of photocatalyst are very important for practical applications. Recycle experiments were therefore carried out to assess the stability of the sample. As displayed in Fig. 7a, the degradation rates of Cr (VI) over $Bi_{.333}(Bi_6S_9)Br$ show a slight decrease after 6 cycles due to incomplete collection and

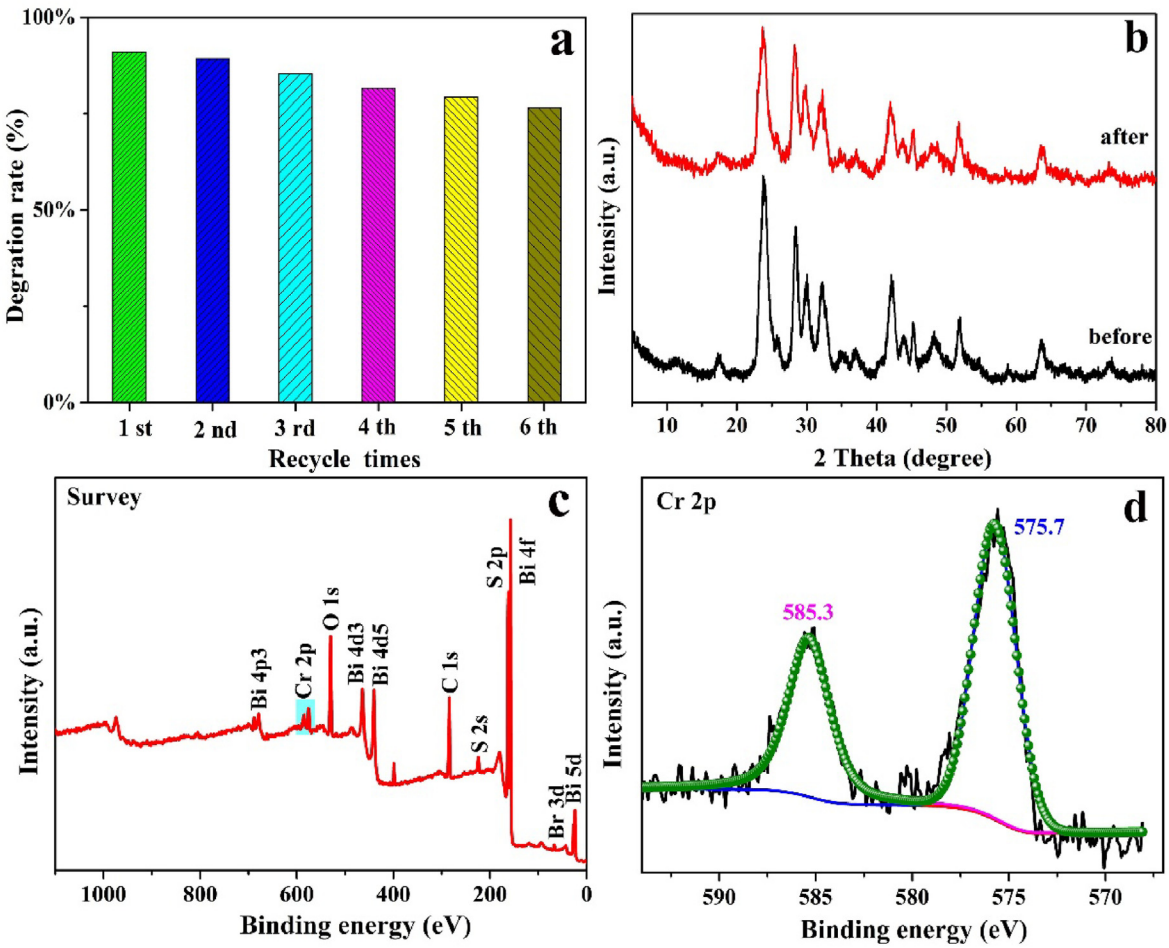

Fig. 7. (a) Degradation rate of Cr (VI) in the presence of $Bi_{.333}(Bi_6S_9)Br$ (obtained at 160 °C for 4 h) under visible light irradiation for 6 cycles; (b) XRD patterns of $Bi_{.333}(Bi_6S_9)Br$ before and after 6 cycles of photocatalytic reaction; XPS analysis of $Bi_{.333}(Bi_6S_9)Br$ after photocatalytic reaction: (c) survey spectrum and (d) Cr 2p spectrum.

washing of the photocatalyst after each cycle. XRD studies revealed no structural change of the sample after photocatalytic tests as indicated by nearly identical diffraction patterns (Fig. 7b). The sample after recycling tests was further characterized by XPS. As shown in Fig. 7c, Bi, Br, S, and Cr were detected in the survey spectrum. In Fig. 7d, the Cr $2p_{3/2}$ and Cr $2p_{1/2}$ peaks were observed at 575.7 and 585.3 eV, respectively, which can be assigned to Cr (III) species [44,45]. The presence of Cr (III) species on the catalyst is obviously due to the successful abatement of Cr (VI) under visible-light illumination.

To understand the photocatalytic performance, PL and EPR spectra of $Bi_{.333}(Bi_6S_9)Br$ were measured and compared with those of BiOBr and Bi_2S_3. PL spectroscopy can be used to evaluate the recombination rate of the photogenerated electrons and holes under irradiation. Fig. 8a shows that the PL intensity of $Bi_{.333}(Bi_6S_9)Br$ is much lower than those of BiOBr and Bi_2S_3, indicating that $Bi_{.333}(Bi_6S_9)Br$ is able to separate photogenerated electrons and holes more effectively. EPR was employed to examine the presence of crystal defects and their relative concentrations in the samples (Fig. 8b). The *g*-factor of $Bi_{.333}(Bi_6S_9)Br$ was determined to be 2.0048, which may be related to the sulfur defects. This is consistent with the XPS results discussed in Fig. 5. Compared to $Bi_{.333}(Bi_6S_9)Br$, the shift of the EPR signal may be attributed to different types of defects [46,47]. In contrast, no signal was detected for Bi_2S_3, indicating that there are little defects. The $Bi_{.333}(Bi_6S_9)Br$ showed a much stronger signal than BiOBr, pointing to the presence of much higher concentration of defects in $Bi_{.333}(Bi_6S_9)Br$. Lots of reports show that the defects can adsorb and activate the pollutants [48–50], which implies more adsorption sites and enhanced reactivity of the $Bi_{.333}(Bi_6S_9)Br$ provided by abundant rationally created surface defects, namely sulfur defects.

Moreover, the reaction intermediates $\cdot OH$ and $\cdot O_2^-$ were measured by ESR, where 5, 5-dimethyl-1-pyrroline-N-oxide (DMPO) was used as the radical scavenger. As described in Fig. 8c and d, both DMPO-$\cdot O_2^-$ (1:1:1:1) and DMPO-$\cdot OH$ (1:2:2:1) signals could not be observed in the dark, while they could be clearly detected under visible light irradiation. Moreover, the illumination time significantly affects the production of $\cdot OH$ and $\cdot O_2^-$. A much higher amount of radicals were detected at 10 min than at 5 min. Considering the band structure of $Bi_{.333}(Bi_6S_9)Br$, the redox abilities of electrons on conduction band (CB) and holes on valence band (VB) are stronger than the potential of $O_2/\cdot O_2^-$ (−0.33 eV) and $HO_2^-/\cdot OH$ (0.12 eV) as well as H_2O_2/O_2 (0.70 eV) [51], respectively. In this case, $\cdot OH$ and $\cdot O_2^-$ radicals can be generated, which is consistent with the results of ESR spin-trap measurements.

Based on these results, a possible photocatalytic reaction mechanism is proposed to elucidate the high photocatalytic activity of $Bi_{.333}(Bi_6S_9)Br$ nanorods (Fig. 9). First, when the $Bi_{.333}(Bi_6S_9)Br$ was irradiated under visible-light, the photogenerated electrons (e^-) were excited from the VB of $Bi_{.333}(Bi_6S_9)Br$ to its CB and the holes (h^+) remained in the VB (Equation (1)). Then, the adsorbed Cr (VI) cations will be reduced rapidly to non-toxic Cr (III) by the

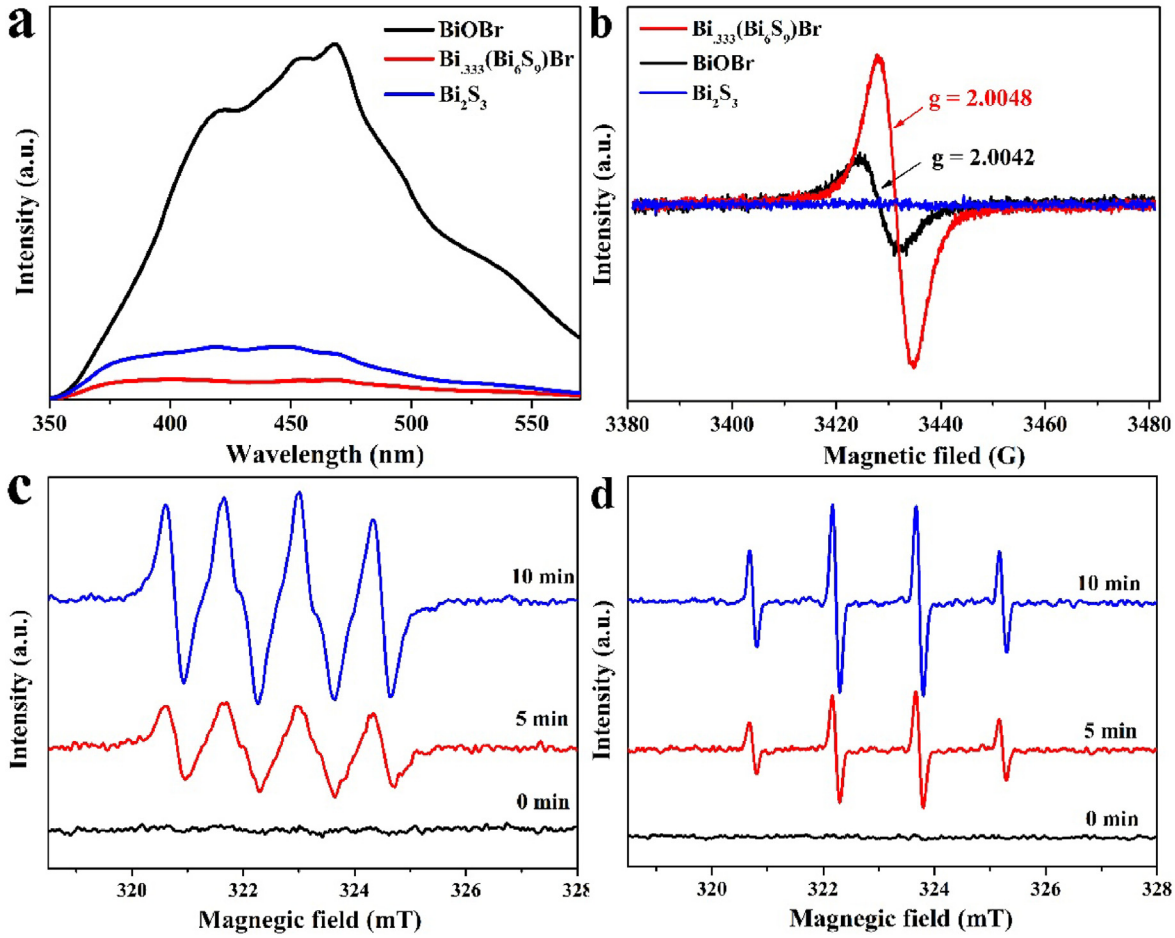

Fig. 8. (a) PL and (b) EPR spectra of the $Bi_{.333}(Bi_6S_9)Br$, BiOBr and Bi_2S_3; ESR spectra of (c) DMPO-·O_2^- and (d) DMPO-·OH using $Bi_{.333}(Bi_6S_9)Br$ as photocatalyst under visible light irradiation for different time (0 min means before irradiation in the dark).

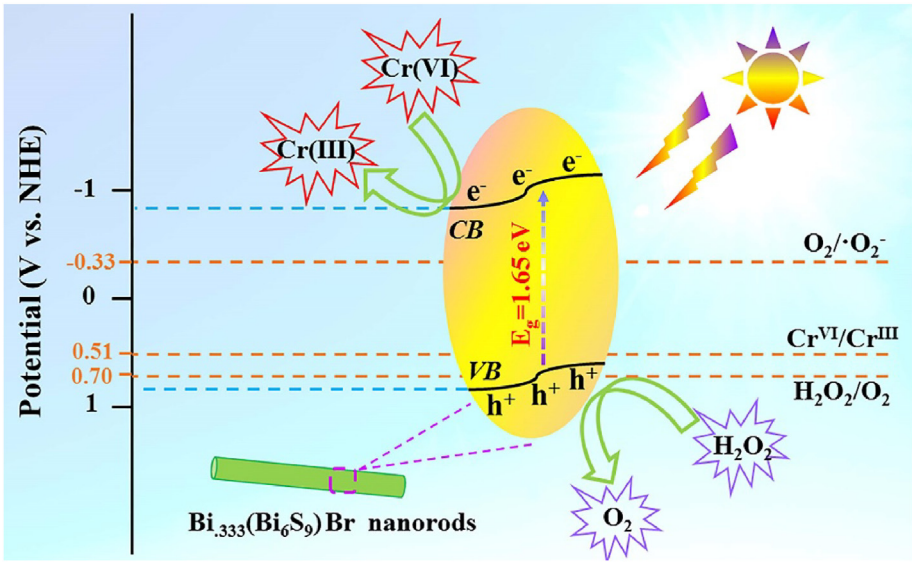

Fig. 9. Schematic diagram of photocatalytic mechanism of $Bi_{.333}(Bi_6S_9)Br$ nanorods.

highly reducing electrons on the CB (Equation (2)), and simultaneously, the H_2O_2 derived from $\cdot OH$ and $\cdot O_2^-$ can be oxidized to O_2 by highly oxidizing holes on the VB, as displayed in Equation (3).

$$Bi_{.333}(Bi_6S_9)Br + h\nu \rightarrow e^- + h^+ \quad (1)$$

$$Cr_2O_7^{2-} + 14\,H^+ + 6e^- \rightarrow 2Cr^{3+} + 7H_2O \quad (2)$$

$$H_2O_2 + 2h^+ \rightarrow O_2 + 2H^+ \quad (3)$$

4. Conclusions

In summary, the single-crystalline hexagonal $Bi_{.333}(Bi_6S_9)Br$ nanorods were successfully synthesized through a hydrothermal route. The morphologies of the as-prepared $Bi_{.333}(Bi_6S_9)Br$ can be easily controlled by varying the hydrothermal reaction time, and a probable formation mechanism was proposed to clarify their growth processes. The obtained $Bi_{.333}(Bi_6S_9)Br$ nanorods have a narrow band gap of about 1.65 eV and a wide light response range, it can effectively inhibit the recombination of photogenerated electrons and holes. The abundant sulfur defects in $Bi_{.333}(Bi_6S_9)Br$ nanorods were beneficial to adsorb and activate Cr (VI), and 90.96% of Cr (VI) was reduced to Cr (III) after 60 min under visible light irradiation. Moreover, the $Bi_{.333}(Bi_6S_9)Br$ nanorods exhibited excellent recyclability and outstanding long-term stability with 76.58% degradation rate of Cr (VI) after six photocatalytic cycles. The photocatalytic reaction mechanism was proposed after considering the results of XPS, EPR, ESR and PL. This dramatically enhanced the photocatalytic activity of the $Bi_{.333}(Bi_6S_9)Br$ nanorods and therefore has promising potential for reducing Cr (VI).

Declaration of competing interest

We declare that we have no financial and personal relationships with other people or organizations that can inappropriately influence our work, there is no professional or other personal interest of any nature or kind in any product, service and/or company that could be construed as influencing the position presented in the manuscript entitled **"Controlled Growth of Single-crystalline $Bi_{.333}(Bi_6S_9)Br$ Nanorods under Hydrothermal Conditions for Enhanced Photocatalytic Reduction of Cr (VI)"**.

CRediT authorship contribution statement

Lili Ai: Data curation, Writing - original draft. **Dianzeng Jia:** Resources, Writing - review & editing, Supervision. **Nannan Guo:** Software, Visualization. **Mengjiao Xu:** Investigation, Methodology. **Su Zhang:** Formal analysis. **Luxiang Wang:** Writing - review & editing, Data curation. **Lixia Jia:** Project administration.

Acknowledgments

This work was supported by the National Program on Key Research Project (2016YFC0400504), the National Science Foundation of China (21671166 and 21701138), the Doctoral Innovation Project of Xinjiang University (XJUBSCX-2017008), and the Autonomous Region Graduate Research Innovation Project (XJ2019G016).

Appendix A. Supplementary data

Supplementary data to this article can be found online at https://doi.org/10.1016/j.jallcom.2020.155879.

References

[1] Z. Wu, Y. Liu, S. Zhang, Z. Huang, Q. Jiang, T. Zhou, J. Hu, Biomimetic structure design and construction of cactus-like $MoS_2/Bi_{19}Cl_3S_{27}$ photocatalysts for efficient hydrogen evolution, J. Mater. Chem. A 6 (2018) 21404–21409.
[2] Z. Wu, Y. Jiang, X. Xiong, S. Ding, Y. Shi, X. Liu, Y. Liu, Z. Huang, J. Hu, Synthesis and characterization of single-crystalline $Bi_{19}Cl_3S_{27}$ nanorods, Catal. Sci. Technol. 7 (2017) 3464–3468.
[3] J. Di, J. Xia, M.F. Chisholm, J. Zhong, C. Chen, X. Cao, F. Dong, Z. Chi, H. Chen, Y. Weng, J. Xiong, S. Yang, H. Li, Z. Liu, S. Dai, Defect-tailoring mediated electron-hole separation in single-unit-cell Bi_3O_4Br nanosheets for boosting photocatalytic hydrogen evolution and nitrogen fixation, Adv. Mater. 31 (2019) 1807576.
[4] X. Jin, C. Lv, X. Zhou, H. Xie, S. Sun, Y. Liu, Q. Meng, G. Chen, A bismuth rich hollow $Bi_4O_5Br_2$ photocatalyst enables dramatic CO_2 reduction activity, Nano Energy 64 (2019) 103955.
[5] J. Ding, Z. Dai, F. Qin, H. Zhao, S. Zhao, R. Chen, Z-scheme $BiO_{1-x}Br/Bi_2O_2CO_3$ photocatalyst with rich oxygen vacancy as electron mediator for highly efficient degradation of antibiotics, Appl. Catal. B Environ. 205 (2017) 281–291.
[6] J. Ding, Z. Dai, F. Tian, B. Zhou, B. Zhao, H. Zhao, Z. Chen, Y. Liu, R. Chen, Generation of defect clusters for $^1O_2$ production for molecular oxygen activation in photocatalysis, J. Mater. Chem. A 5 (2017) 23453–23459.
[7] Y. Guo, Y. Ao, P. Wang, C. Wang, Mediator-free direct dual-Z-scheme $Bi_2S_3/BiVO_4/MgIn_2S_4$ composite photocatalysts with enhanced visible-light-driven performance towards carbamazepine degradation, Appl. Catal. B Environ. 254 (2019) 479–490.
[8] R. Liang, F. Jing, L. Shen, N. Qin, L. Wu, M@ MIL-100 (Fe)(M= Au, Pd, Pt) nanocomposites fabricated by a facile photodeposition process: efficient visible-light photocatalysts for redox reactions in water, Nano Res. 8 (2015) 3237–3249.
[9] R. Liang, L. Shen, F. Jing, N. Qin, L. Wu, Preparation of MIL-53 (Fe)-reduced graphene oxide nanocomposites by a simple self-assembly strategy for increasing interfacial contact: efficient visible-light photocatalysts, ACS Appl. Mater. Interfaces 7 (2015) 9507–9515.
[10] R. Liang, L. Shen, F. Jing, W. Wu, N. Qin, R. Lin, L. Wu, NH_2-mediated indium metal-organic framework as a novel visible-light-driven photocatalyst for reduction of the aqueous Cr (VI), Appl. Catal. B Environ. 162 (2015) 245–251.
[11] Y. Shi, X. Xiong, S. Ding, X. Liu, Q. Jiang, J. Hu, In-situ topotactic synthesis and photocatalytic activity of plate-like BiOCl/2D networks Bi_2S_3 heterostructures, Appl. Catal. B Environ. 220 (2018) 570–580.
[12] Y. Li, Y. Fu, M. Zhu, Green synthesis of 3D tripyramid TiO_2 architectures with assistance of aloe extracts for highly efficient photocatalytic degradation of antibiotic ciprofloxacin, Appl. Catal. B Environ. 260 (2020) 118149.
[13] Y. Wang, L. Rao, P. Wang, Z. Shi, L. Zhang, Photocatalytic activity of N-TiO_2/O-doped N vacancy g-C_3N_4 and the intermediates toxicity evaluation under tetracycline hydrochloride and Cr (VI) coexistence environment, Appl. Catal. B Environ. 262 (2020) 118308.
[14] B. Li, L. Shao, R. Wang, X. Dong, F. Zhao, P. Gao, Z. Li, Interfacial synergism of Pd-decorated BiOCl ultrathin nanosheets for the selective oxidation of aromatic alcohols, J. Mater. Chem. A 6 (2018) 6344–6355.
[15] H. Wang, W. Zhang, X. Li, J. Li, W. Cen, Q. Li, F. Dong, Highly enhanced visible light photocatalysis and in situ FT-IR studies on Bi metal@defective BiOCl hierarchical microspheres, Appl. Catal. B Environ. 225 (2018) 218–227.
[16] M. Guan, C. Xiao, J. Zhang, S. Fan, R. An, Q. Cheng, J. Xie, M. Zhou, B. Ye, Y. Xie, Vacancy associates promoting solar-driven photocatalytic activity of ultrathin bismuth oxychloride nanosheets, J. Am. Chem. Soc. 135 (2013) 10411–10417.
[17] H. Wang, D. Yong, S. Chen, S. Jiang, X. Zhang, W. Shao, Q. Zhang, W. Yan, B. Pan, Y. Xie, Oxygen-vacancy-mediated exciton dissociation in BiOBr for boosting charge-carrier-involved molecular oxygen activation, J. Am. Chem. Soc. 140 (2018) 1760–1766.
[18] X. Zhou, C. Shao, S. Yang, X. Li, X. Guo, X. Wang, X. Li, Y. Liu, Heterojunction of g-C_3N_4/BiOI immobilized on flexible electrospun polyacrylonitrile nanofibers: facile preparation and enhanced visible photocatalytic activity for floating photocatalysis, ACS Sustain. Chem. Eng. 6 (2018) 2316–2323.
[19] N. Han, Y. Wang, H. Yang, J. Deng, J. Wu, Y. Li, Y. Li, Ultrathin bismuth nanosheets from in situ topotactic transformation for selective electrocatalytic CO_2 reduction to formate, Nat. Commun. 9 (2018) 1–8.
[20] Z. Jia, T. Li, Z. Zheng, J. Zhang, J. Liu, R. Li, Y. Wang, X. Zhang, Y. Wang, C. Fan, The BiOCl/diatomite composites for rapid photocatalytic degradation of ciprofloxacin: efficiency, toxicity evaluation, mechanisms and pathways, Chem. Eng. J. 380 (2020) 122422.
[21] J. Zhong, Y. Zhao, L. Ding, H. Ji, W. Ma, C. Chen, J. Zhao, Opposite photocatalytic oxidation behaviors of BiOCl and TiO_2: direct hole transfer vs. indirect OH oxidation, Appl. Catal. B Environ. 241 (2019) 514–520.
[22] X. Gao, G. Tang, W. Peng, Q. Guo, Y. Luo, Surprise in the phosphate modification of BiOCl with oxygen vacancy: in situ construction of hierarchical Z-scheme BiOCl-OV-$BiPO_4$ photocatalyst for the degradation of carbamazepine, Chem. Eng. J. 360 (2019) 1320–1329.
[23] S. Luo, F. Qin, Y. Ming, H. Zhao, Y. Liu, R. Chen, Fabrication uniform hollow Bi_2S_3 nanospheres via Kirkendall effect for photocatalytic reduction of Cr (VI) in electroplating industry wastewater, J. Hazard Mater. 340 (2017) 253–262.
[24] J. Jin, T. He, Facile synthesis of Bi_2S_3 nanoribbons for photocatalytic reduction of CO_2 into CH_3OH, Appl. Surf. Sci. 394 (2017) 364–370.
[25] R. Wang, G. Cheng, Z. Dai, J. Ding, Y. Liu, R. Chen, Ionic liquid-employed

synthesis of Bi_2E_3 (E= S, Se, and Te) hierarchitectures: the case of Bi_2S_3 with superior visible-light-driven Cr (VI) photoreduction capacity, Chem. Eng. J. 327 (2017) 371–386.
[26] H. Kunioku, M. Higashi, R. Abe, Low-temperature synthesis of bismuth chalcohalides: candidate photovoltaic materials with easily, continuously controllable band gap, Sci. Rep. 6 (2016) 32664.
[27] Z. Ran, X. Wang, Y. Li, D. Yang, X. Zhao, K. Biswas, D. Singh, L. Zhang, Bismuth and antimony-based oxyhalides and chalcohalides as potential optoelectronic materials, npj Comput. Mater. 4 (2018) 1–7.
[28] P. Wen, L. Ai, T. Liu, D. Hu, F. Yao, Hydrothermal topological synthesis and photocatalyst performance of orthorhombic Nb_2O_5 rectangle nanosheet crystals with dominantly exposed (010) facet, Mater. Des. 117 (2017) 346–352.
[29] H. Sun, Z. Jiang, D. Wu, L. Ye, T. Wang, B. Wang, T. An, P. Wong, Defect-type-dependent near-infrared-driven photocatalytic bacterial inactivation by defective Bi_2S_3 nanorods, ChemSusChem 12 (2019) 890–897.
[30] J. Zhang, L. Zhang, N. Yu, K. Xu, S. Li, H. Wang, J. Liu, Flower-like Bi_2S_3/Bi_2MoO_6 heterojunction superstructures with enhanced visible-light-driven photocatalytic activity, RSC Adv. 5 (2015) 75081–75088.
[31] J. Di, J. Xia, M. Ji, S. Yin, H. Li, H. Xu, Q. Zhang, H. Li, Controllable synthesis of $Bi_4O_5Br_2$ ultrathin nanosheets for photocatalytic removal of ciprofloxacin and mechanism insight, J. Mater. Chem. A 3 (2015) 15108–15118.
[32] W. Chai, F. Yang, W. Yin, S. You, K. Wang, W. Ye, Y. Rui, B. Tang, Bi_2S_3/C nanorods as efficient anode materials for lithium-ion batteries, Dalton Trans. 48 (2019) 1906–1914.
[33] Y. Cheng, Y. Chang, Y. Feng, H. Jian, Z. Tang, H. Zhang, Deep-level defect enhanced photothermal performance of bismuth sulfide-gold heterojunction nanorods for photothermal therapy of cancer guided by computed tomography imaging, Angew. Chem. Int. Ed. 57 (2018) 246–251.
[34] Z. Liu, D. Xiao, H. Huang, J. Zhang, C. Niu, Carve designs of MoS_2 nanostructures by controlling 3D MoS_2 nanomasks, Inorg. Chem. Front. 5 (2018) 2598–2604.
[35] S. Mao, R. Bao, D. Fang, J. Yi, Facile synthesis of Ag/AgX (X= Cl, Br) with enhanced visible-light-induced photocatalytic activity by ultrasonic spray pyrolysis method, Adv. Powder Technol. 29 (2018) 2670–2677.
[36] X. Tang, Z. Wang, N. Wu, S. Liu, N. Liu, A novel visible-light-active β-Bi_2O_3/BiOBr heterojunction photocatalyst with remarkably enhanced photocatalytic activity, Catal. Commun. 119 (2019) 119–123.
[37] W. Zheng, W. Jia, L. Deng, B. Wang, Y. Tian, A. Zhang, L. Mao, J. Liu, W. Zhang, Towards unique shear thinning behaviors under electric and magnetic fields achieved by TiO_2 decorated magnetic MoS_2 nanosheets: lubricating effects, J. Mater. Chem. C 6 (2018) 1836–1843.
[38] R. Gupta, S. Sen, D. Phase, D. Avasthi, A. Gupta, Tailoring optical properties of TiO_2-Cr co-sputtered films using swift heavy ions, Appl. Surf. Sci. 440 (2018) 403–408.
[39] P. Shandilya, D. Mittal, M. Soni, P. Raizada, A. Hosseini-Bandegharaei, A. Saini, P. Singh, Fabrication of fluorine doped graphene and $SmVO_4$ based dispersed and adsorptive photocatalyst for abatement of phenolic compounds from water and bacterial disinfection, J. Clean. Prod. 203 (2018) 386–399.
[40] P. Shandilya, D. Mittal, M. Soni, P. Raizada, J. Lim, D. Jeong, R. Dewedi, A. Saini, P. Singh, Islanding of $EuVO_4$ on high-dispersed fluorine doped few layered graphene sheets for efficient photocatalytic mineralization of phenolic compounds and bacterial disinfection, J. Taiwan Inst. Chem. Eng. 93 (2018) 528–542.
[41] P. Singh, P. Shandilya, P. Raizada, A. Sudhaik, A. Rahmani-Sani, A. Hosseini-Bandegharaei, Review on various strategies for enhancing photocatalytic activity of graphene based nanocomposites for water purification, Arab. J. Chem. 13 (2020) 3498–3520.
[42] A. Kumar, P. Raizada, P. Singh, R. Saini, A. Saini, A. Hosseini-Bandegharaei, Perspective and status of polymeric graphitic carbon nitride based Z-scheme photocatalytic systems for sustainable photocatalytic water purification, Chem. Eng. J. (2019) 123496.
[43] P. Shandilya, D. Mittal, A. Sudhaik, M. Soni, P. Raizada, A. Saini, P. Singh, $GdVO_4$ modified fluorine doped graphene nanosheets as dispersed photocatalyst for mitigation of phenolic compounds in aqueous environment and bacterial disinfection, Separ. Purif. Technol. 210 (2019) 804–816.
[44] M. Luo, Y. Xiong, H. Wu, X. Feng, J. Li, F. Luo, The MOF^+ technique: a significant synergic effect enables high performance chromate removal, Angew. Chem. Int. Ed. 56 (2017) 16376–16379.
[45] K. Li, Z. Huang, S. Zhu, S. Luo, L. Yan, Y. Dai, Y. Guo, Y. Yang, Removal of Cr (VI) from water by a biochar-coupled g-C_3N_4 nanosheets composite and performance of a recycled photocatalyst in single and combined pollution systems, Appl. Catal. B Environ. 243 (2019) 386–396.
[46] F. Li, Z. Chang, K. Khaing, Y. Zhou, H. Zhao, N. Liang, D. Zhou, B. Pan, C. Steinberg, Organic matter protection by kaolinite over bio-decomposition as suggested by lignin and solvent-extractable lipid molecular markers, Sci. Total Environ. 647 (2019) 570–576.
[47] T. Xia, W. Zhang, J. Murowchick, G. Liu, X. Chen, A facile method to improve the photocatalytic and lithium-ion rechargeable battery performance of TiO_2 nanocrystals, Adv. Energy Mater. 3 (2013) 1516–1523.
[48] H. Yu, J. Li, Y. Zhang, S. Yang, K. Han, F. Dong, T. Ma, H. Huang, Three-in-one oxygen vacancies: whole visible-spectrum absorption, efficient charge separation, and surface site activation for robust CO_2 photoreduction, Angew. Chem. Int. Ed. 58 (2019) 3880–3884.
[49] Y. Liu, C. Miao, P. Yang, Y. He, J. Feng, D. Li, Synergetic promotional effect of oxygen vacancy-rich ultrathin TiO_2 and photochemical induced highly dispersed Pt for photoreduction of CO_2 with H_2O, Appl. Catal. B Environ. 244 (2019) 919–930.
[50] X. Kong, B. Ng, K. Tan, X. Chen, H. Wang, A. Mohamed, S. Chai, Simultaneous generation of oxygen vacancies on ultrathin BiOBr nanosheets during visible-light-driven CO_2 photoreduction evoked superior activity and long-term stability, Catal. Today 314 (2018) 20–27.
[51] X. Qiao, Z. Zhang, Q. Li, D. Hou, Q. Zhang, J. Zhang, D. Li, P. Feng, X. Bu, In situ synthesis of n-n Bi_2MoO_6 & Bi_2S_3 heterojunctions for highly efficient photocatalytic removal of Cr (VI), J. Mater. Chem. A 6 (2018) 22580–22589.